Road marking BRDF model applicable for a wide range of incident illumination conditions

Journal of the Optical Society of America A
OPTICS, IMAGE SCIENCE, AND VISION

Road marking BRDF model applicable for a wide range of incident illumination conditions

Rik Marco Spieringhs,[1,2,*] Jan Audenaert,[1] Kevin Smet,[1] Ingrid Heynderickx,[2] and Peter Hanselaer[1]

[1]KU Leuven, ESAT/Light & Lighting Laboratory, Gebroeders De Smetstraat 1, 9000 Ghent, Belgium
[2]TU Eindhoven, IEIS/Human Technology Interaction, De Zaale 1, 5600MB Eindhoven, The Netherlands
*rik.spieringhs@kuleuven.be

Received 19 July 2022; revised 20 December 2022; accepted 26 January 2023; posted 26 January 2023; published 24 February 2023

To drive safely and comfortably, an adequate contrast between the road surface and road markings is needed. This contrast can be improved by using optimized road illumination designs and luminaires with dedicated luminous intensity distributions, taking advantage of the (retro)reflective characteristics of the road surface and road markings. Since little is known about road markings' (retro)reflective characteristics for the incident and viewing angles relevant for street luminaires, bidirectional reflectance distribution function (BRDF)-values of some retroreflective materials are measured for a wide range of illumination and viewing angles using a luminance camera in a commercial near-field goniophotometer setup. The experimental data are fitted to a new and optimized "*RetroPhong*" model, which shows good agreement with the data [root mean squared error (RMSE) < 0.13, normalized root mean squared error (NRMSE) < 0.04, and the normalized cross correlation ratio (NCC) > 0.8]. The RetroPhong model is benchmarked with other relevant (retro)reflective BRDF models, and the results suggest that the RetroPhong model is most suitable for the current set of samples and measurement conditions.

https://doi.org/10.1364/JOSAA.470968

1. INTRODUCTION

Retroreflective materials have the property that they also reflect light in directions close to the incident light direction. For this reason, retroreflective materials are intensively used in road signaling to increase safety while driving at night time when car headlamps are the main illumination source. Both vertically oriented road signs and horizontal road markings make use of these retroreflective properties for improving road signalization, while retroreflective textiles and strips improve the visibility of pedestrians and cyclists. Retroreflective properties of materials are created by adding glass beads in the substrate, such as in road markings and textiles, or by using prismatic foils (as used in road signals) [1]. The retroreflective behavior is due to specular reflection, refraction, and total internal reflection.

Because good visibility of objects and signs is crucial to prevent accidents and to guide traffic, controlling and improving the retroreflective properties of materials in different weather conditions is an important objective for material manufacturers. Currently, the requirements for the optical characteristics of retroreflective materials are formulated in dedicated standards and documents, namely CIE 54.2 [2] and EN1436 [3] for road markings, CIE 74 [4] and EN12899 [5] for road signs, and EN20471 [6] for high visibility clothing. These standards specify the retroreflective properties for dedicated directions of illumination and viewing, in terms of the coefficient of retroreflection R_A and coefficient of retroreflected luminance R_l, which are defined as the quotient of the luminous intensity reflected by the material in the standardized angular direction and the surface illuminance multiplied by its area, and the quotient of the luminous intensity reflected by the material in the standardized angular direction and the surface illuminance multiplied by its projected area, respectively.

Currently, these retroreflective materials are optimized under the assumption that only car headlights interact with these materials, limiting the range of the incident angles of the illumination. Traditional road lighting is not designed to contribute to the retroreflection of these materials. However, a road lighting concept called "*Probeam*" [7,8] shows promising advantages over other, more common, road lighting concepts such as symmetrical road lighting. With Probeam, luminaires direct most of their luminous flux forward parallel to the driving direction; as such, their light contribution might become relevant at distances beyond the reach of car headlights. Consequently, the range of incident and viewing angles with respect to the retroreflective materials becomes quite different from the range of angles involved when only car headlights are taken into consideration. Unfortunately, the retroreflective characteristics of road markings and signals are not available for this extended range of incident angles. This lack of data hampers a qualitative

and quantitative analysis of alternative lighting concepts, and makes it impossible to make accurate renderings of the scene as observed by the driver.

In general, the reflection properties of a material for different viewing angles and different angles of incident of the light are described by the bidirectional reflectance distribution function, or shortly BRDF [9]. Typically, a photometric BRDF is determined as the ratio between the elementary luminance in a particular viewing angle (dL) and the elementary illuminance measured on a surface of the material from a particular incident direction (dE). Mathematically the BRDF is defined as follows:

$$f_r(\theta_i, \varphi_i, \theta_o, \varphi_o) = \frac{dL(\theta_o, \varphi_o)}{dE(\theta_i, \varphi_i)}, \tag{1}$$

where f_r represents the BRDF in sr^{-1}, θ_i the polar angle of incidence, φ_i the azimuth angle of incidence, θ_o the polar angle of viewing, φ_o the azimuth angle of viewing (with all angles expressed in degrees), L the luminance, and E the illuminance. The polar coordinate is defined toward the external normal of the sample, while the azimuthal coordinate is defined toward a two-dimensional coordinate system within the sample surface. BRDF is a function used to provide a complete indication of the reflection characteristics of a material. For special applications, such as the description of the retroreflectivity of a material at standardized angles, secondary quantities such as R_A and R_I are used.

To determine a complete BRDF dataset experimentally is quite time consuming due to its four-dimensional nature. One way of handling this huge amount of data is to fit the data to a suitable analytical model, of which its parameters are optimized to the data. These models are also necessary to import material characteristics in physical-based renderers (PBRs) [10]. Several analytical BRDF models can be found in literature [11], but there is a lack of BRDF models including retroreflection. Belcour *et al*. [10] suggested a set of updated and improved parametric BRDF models (i.e., updated Blinn, updated Beckmann, updated ABC distribution, and the Lafortune model) that include retroreflection. They measured gray, yellow, and orange retroreflective tape, typically used in safety jackets, for a few incident angles (i.e., $\theta_i = 15°, 30°, 60°$) and many viewing angles. However, these updated and improved parametric BRDF models have not yet been applied to glass-bead-based retroreflective road markings.

In this study, first, BRDF values of retroreflective road markings are derived from measurements at multiple incident and viewing angles more relevant to road lighting (i.e., luminaires), and different from the traditional incident and viewing angles mentioned in CIE 54.2 [2] for road lighting by car headlights (i.e., $\theta_i, \varphi_i, \theta_o$, and φ_o, are 88.8°, 0°, 87.7°, and 0°, respectively). These measurements, thereafter, are used to develop a new retroreflective BRDF model. The developed model is then benchmarked against existing parametric retroreflective BRDF models. The new BRDF model can lead to new insights in the visibility of retroreflective road markings at a broader range of incident angles and can lead to a more qualitative and quantitative analysis of new road lighting designs such as Probeam, which make optimal use of these retroreflective characteristics.

2. BRDF MODELS

This section gives a short overview of various existing BRDF models that are used later in this paper to fit our experimental data.

A. Classic Phong Model

The classic Phong model is one of the most well-known and popular BRDF models used in computer graphics because of its simplicity and relatively low computational cost. The classic Phong model is categorized as an empirical BRDF model that does not account for energy conservation and reciprocity. The model contains an exponential parameter n for the "shininess" of the material (i.e., a large n generally indicates a large specular highlight), a parameter for the diffuse reflection k_d, and a parameter for the specular reflection k_s,

$$f_r(\theta_i, \varphi_i, \theta_o, \varphi_o) = \frac{k_d}{\pi} + k_s(i_s \cdot o)^n, \tag{2}$$

in which i_s is the specular reflection unit vector in the direction of $\varphi_i + \pi$, and o is the unit vector in the direction of the viewer.

The model is often modified for energy conservation using the approach introduced by Lafortune [11], with k_d and k_s fulfilling the constraint $k_d + k_s < 1$, as shown in Eq. (3),

$$f_r(\theta_i, \varphi_i, \theta_o, \varphi_o) = \frac{k_d}{\pi} + \frac{k_s(n+2)}{2\pi}(i_s \cdot o)^n. \tag{3}$$

B. BRDF Models Including Retroreflection

The Beckmann distribution model refers to the assumption that the distribution of the microfacet normals follows a normal distribution, asserting that real material surfaces can be represented using microfacets with different orientations. The Beckmann model is determined by a Fresnel term F (fraction of light that is reflected from an entire surface), a geometric attenuation factor G (factor describing the effect of masking), and the distribution of microfacets D,

$$f_r(i, o, n) = \frac{F(o \cdot h_r)G(i, o, h_r)\, D(h_r)}{4 \cdot |i \cdot n||o \cdot n|}, \tag{4}$$

where h_r the half-way vector (between i and o), and n is the normal vector. A more detailed description of the factors F, G, and D is given by Smith [12], Beckmann and Spizzichino [13], Schlick [14], and Belcour *et al*. [10]. The updated Beckmann model, here called Beckmann-Retro model and formulated by Belcour *et al*. [10], is different from the original model with respect to the inputs of the factors F and G; furthermore, an alternative microfacet distribution D_b is introduced,

$$f_b(i, o, n) = \frac{F(o' \cdot b)G(i, o, h_r)\, D_b(b)}{4 \cdot |i \cdot n||o \cdot n|}, \tag{5}$$

where o' is the vector in the opposite direction of the viewer and b is the so-called back vector, which is the half-way vector between i and o'. The altered microfacet distribution including retroreflection is given by

$$D_b(b) = \frac{1}{\pi\alpha^2\cos(b \cdot n)^4} e^{\frac{\cos(b \cdot n)^2 - 1}{\alpha^2 \cos(b \cdot n)^2}}, \tag{6}$$

where b is the back vector, n is the normal, and α is a parameter for the apparent roughness for retroreflection.

Furthermore, the Schlick's approximation of the Fresnel term is adopted,

$$F(o \cdot h_r) = \left(\frac{\eta_1 - \eta_2}{\eta_1 + \eta_2}\right)^2 + \left(1 - \left(\frac{\eta_1 - \eta_2}{\eta_1 + \eta_2}\right)^2\right) \times (1 - \cos(o \cdot h_r))^5, \quad (7)$$

where η_1 is the refractive index of medium 1 and η_2 is the refractive index of medium 2.

The Blinn model [15] is a quite simple cosine model. It exists of the dot product between the half-way vector h_r and the surface normal vector n,

$$f_r = (h_r \cdot n)^\alpha, \quad (8)$$

with α a power factor that is related to the "shininess" of the material. The Blinn model was extended to include retroreflection (Blinn-Retro model) by simply replacing the half-way vector with the back vector [10],

$$f_b = (b \cdot n)^\alpha. \quad (9)$$

The third model, the (original) ABC model, was first introduced in 1989 by Church *et al*. [16] based on the Raleigh–Rice theory. It was later adapted by Löw *et al*. in 2012 [17] to derive a new microfacet BRDF model,

$$f_r = \frac{A}{(1 + B(1 - (o \cdot h_r)))^C} F(o \cdot h_r), \quad (10)$$

where A, B, and C are parameters (referring to the ABC model) and F is the Fresnel term; A is a general scaling parameter, whereas B and C determine the width of the specular peak and falloff rate of the wide-angle scattering, respectively. This model was further modified to include retroreflection (ABC-Retro model) by Belcour *et al*. in 2014 [10],

$$f_b = \frac{A}{(1 + B(1 - \cos B))^C} F(o' \cdot b). \quad (11)$$

3. MEASUREMENT SETUP

The BRDF measurements were performed with a large near-field goniometer (LNFG) manufactured by TechnoTeam, shown in Fig. 1. Typically, the LNFG is used for measuring luminaires based on near-field luminance camera recordings for which the luminaire is placed at the center of the goniometer. For the BRDF measurements, the setup was altered as shown in Fig. 1, where a sample was placed in the center and an external light source was added at a fixed position.

The measurement setup consists of three elements: the (additional) light source, the holder for the test object, and the luminance camera. The light source, shown in the red frame of Fig. 1, consists of a QTH10(/M) Quartz Tungsten-Halogen 50 W 12 V lamp with a broadband emission between 400 and 2200 nm and connected to a programmable Delta Elektronika SM1500 DC power system. An optical system consisting of a lens and two Newport M-ID-1.5 iris diaphragms projects a circular light spot with a diameter of 7.5 cm at the test sample

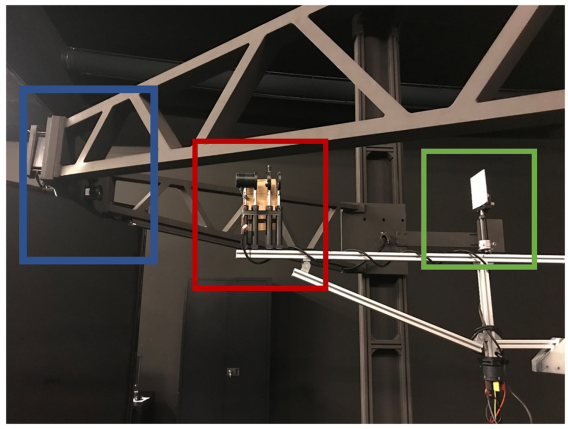

Fig. 1. Measurement setup where the blue box indicates the luminance camera, the red box the fixed light source, and the green box the sample and sample holder.

Fig. 2. Photograph of the sample and sample holder, showing the circular light spot with a diameter of 7.5 cm on the test sample at perpendicular incident.

when the illumination is perpendicular to the sample. In the measurement setup, a halogen light source is used as illuminant (as also used in EN1436), although in road lighting typically LED light sources are used. In principle, the photometric BRDF is dependent on the spectral distribution of the illuminant. However, the spectral reflectance of road markings shows almost no dependency on wavelength (neutral samples); as such, the impact of the spectral distribution of the illuminant on the photometric BRDF values is negligible. The light spot can be seen more clearly in Fig. 2. The whole optical system is mounted on a dedicated lever and is fixed in that position.

The sample holder, shown in the green frame of Fig. 2, is adjustable and can be rotated around both a vertical and horizontal axis in such a way that any incident angle (θ, φ) can be selected.

The camera, shown in the blue box of Fig. 1, consists of a TechnoTeam LMK 98-4 high-tech calibrated luminance camera with a resolution of 1390 × 1040 pixels and is mounted in

Fig. 3. Photographs taken from the three test samples: (1) SWARCO Limboplast D480 with Megalux 0.6-1.5 KT14, (2) SWARCO Limboplast D480 with P21 3:1, and (3) 3M Stamark A650.

the RIGO801 LNFG. The RIGO801 LNFG can move freely so that all desired viewing angles can be measured.

The camera and the RIGO801 LNFG are linked to a computer so that the position of the arm of the LNFG can be set via the TechnoTeam software and luminance images are recorded. After each series of measurements, the illuminance on the test sample was measured at perpendicular incidence with a Gigahertz Optik Optometer P9710 and stored in a text file. The illuminance at non-normal incident angles was calculated by multiplying the measured illuminance with the cosine of the incident polar angle.

4. MEASUREMENT GEOMETRY

Three road marking cutout test samples containing glass beads are considered and shown in Fig. 3:

1. SWARCO Limboplast D480 with Megalux 0.6-1.5 KT14
2. SWARCO Limboplast D480 with P21 3:1
3. 3M Stamark A650

In Fig. 4, the geometry of the measurement system is shown. A fixed global XYZ coordinate system (GCS) is defined with the Z axis vertically and with the origin at the center of the LNFG. A sample coordinate system (SCS) is defined with the local z axis aligned with the normal to the retroreflector, and the local x and y axes are marked on the sample to form a right-handed coordinate system. If the sample is positioned appropriately, the origin of the SCS coincides with the origin of the GCS. The illumination system aperture is positioned at (X, Y, Z) = (0, −0.92, 0), and the direction of the fixed incident beam (L_i) is parallel to the Y direction.

In the home position, the sample is oriented with the z axis parallel to the minus Y axis and the x axis parallel to the X axis; this situation corresponds to an incident angle $\theta_i = 0°$. The home position of the camera is at (X, Y, Z) = (0, 0, 1.54), corresponding to a viewing angle of $\theta_o = 90°$ and $\varphi_0 = 90°$. The incident angles can be changed by rotating the sample normal (z axis) around the vertical Z axis in the positive direction over an angle θ_i. Rotating the sample around the new z axis allows us to change φ_i. The viewing angles can be changed by rotating the

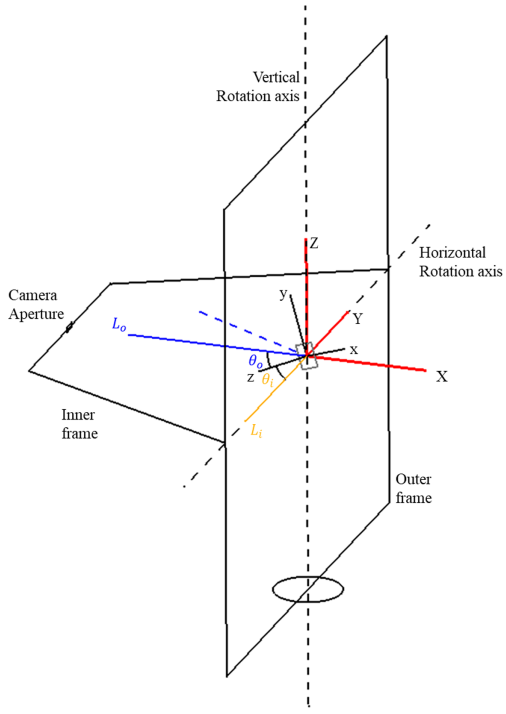

Fig. 4. Overview of the local (black x, y, z) and global (red X, Y, Z) coordinate system within the LNFG; the direction of the incident light is shown as L_i (orange).

camera around the horizontal Y axis and the vertical Z axis of the goniometer.

The new positions of the SCS axes and the camera position vector (L_o) after the rotations can be found by applying the general formula for a rotation of a vector B around a vector A over an angle α given by [18]

$$B' = rm(A, \alpha) \cdot B, \tag{12}$$

with B' being the rotated position of B and the rotation matrix $rm(A, \alpha)$ given by

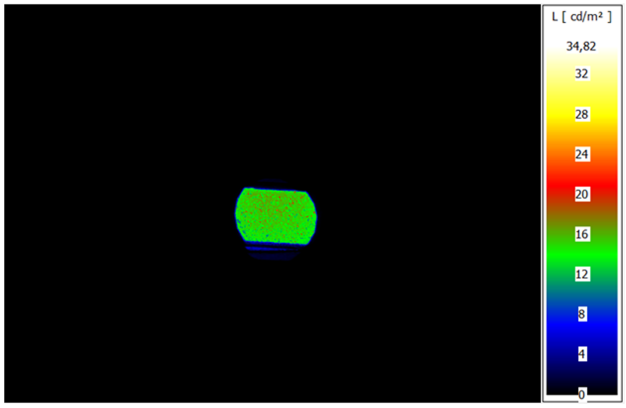

Fig. 5. Luminance image of road marking 1 for an angle of incidence (θ_i, φ_i) of (0°,0°) and a viewing angle (θ_o, φ_o) of (21°,51°).

Table 1. Selected θ Angles of Incident for Each Selected φ Angle of Incidence in Degrees

Incident Angles	
φ_i	θ_i
0	0, 10, 20, 30, 40, 50, 60, 70, 80, 85
23	70, 80, 85
45	70, 80, 85

Table 2. Selected θ Viewing Angles Chosen for Each Selected φ Viewing Angle in Degrees, for an Angle of Incidence of $\varphi_i = 0°$ and $\theta_i = 0°$

Viewing Angles	
φ_o	θ_o
25.7	3.3, 10.7, 21.3, 34.8, 50.8, 69.3
51.4	3.3, 10.7, 21.3, 34.8, 50.8, 69.3
77.1	3.3, 10.7, 21.3, 34.8, 50.8, 69.3
102.9	3.3, 10.7, 21.3, 34.8, 50.8, 69.3
128.6	3.3, 10.7, 21.3, 34.8, 50.8, 69.3
154.3	3.3, 10.7, 21.3, 34.8, 50.8, 69.3
180	3.3, 10.7, 21.3, 34.8, 50.8, 69.3
205.7	3.3, 10.7, 21.3, 34.8, 50.8, 69.3
231.4	3.3, 10.7, 21.3, 34.8, 50.8, 69.3
257.1	3.3, 10.7, 21.3, 34.8, 50.8, 69.3
282.9	3.3, 10.7, 21.3, 34.8, 50.8, 69.3
308.6	3.3, 10.7, 21.3, 34.8, 50.8, 69.3
334.3	3.3, 10.7, 21.3, 34.8, 50.8, 69.3
360	3.3, 10.7, 21.3, 34.8, 50.8, 69.3

$$rm(A,\alpha)=\frac{1}{|A|}\begin{pmatrix} A_x^2+\cos\alpha(A_y^2+A_z^2) & A_xA_y(1-\cos\alpha)-A_z|A|^{\frac{1}{2}}\sin\alpha & A_xA_z(1-\cos\alpha)+A_y|A|^{\frac{1}{2}}\sin\alpha \\ A_xA_y(1-\cos\alpha)+A_z|A|^{\frac{1}{2}}\sin\alpha & A_y^2+\cos\alpha(A_x^2+A_z^2) & A_yA_z(1-\cos\alpha)-A_x|A|^{\frac{1}{2}}\sin\alpha \\ A_xA_z(1-\cos\alpha)+A_y|A|^{\frac{1}{2}}\sin\alpha & A_yA_z(1-\cos\alpha)+A_x|A|^{\frac{1}{2}}\sin\alpha & A_z^2+\cos\alpha(A_x^2+A_y^2) \end{pmatrix}. \tag{13}$$

This equation can be used for each rotation involved. Once a new position vector is known in the GCS, the spherical coordinates toward the SCS can be calculated.

As discussed previously, HDR luminance images of the sample were taken at different viewing angles for different angles of incident. An example of such a luminance image can be seen in Fig. 5. After applying a dark correction, the average luminance of a group of central pixels (70 pixels × 70 pixels), belonging to the area of the road marking that is illuminated, was calculated. This luminance was then divided by the illuminance at the chosen angle of incidence to determine the BRDF value for that specific angle of incidence and viewing.

A wide variety of incident angles was chosen to get a good idea of the reflection properties of the road markings. The selected incident angles can be found in Table 1. For a φ_i of 0°, the θ_i angles were equally spaced between 0° and 90°, but with 90° substituted by 85°. Angles θ_i above 85° are less important when considering conditions of illumination by luminaires, and they are much more difficult to measure given the current setup. To check the angular dependence of the reflectivity on φ_i, a φ_i of 23° and 45° were included where only the more relevant θ_i angles of 70°, 80°, and 85° were used. For each incident angle, a wide variety of viewing angles was chosen with a higher concentration around the incident angle to measure the retroreflectivity in more detail. The viewing angles are shown in Table 2 for the angle of incidence $\varphi_i = 0°$ and $\theta_i = 0°$.

Note that the illumination and viewing angles mentioned in Table 1 and Table 2 have been selected according to the situation we are targeting, i.e., the illumination of the road and road signs by the road luminaires and observation of the reflected light by the car driver.

5. MEASUREMENT DATA

For each incident angle, the BRDF value was determined for all viewing angles, a visualization of which is shown in Fig. 6 for one particular angle of incidence. The BRDF value at each measured viewing angle (represented by a dot) is relative to the length of the incident vector (represented by the red dashed line with length 1). The large BRDF values in the direction of incidence indicate the retroreflective character of the road marking material.

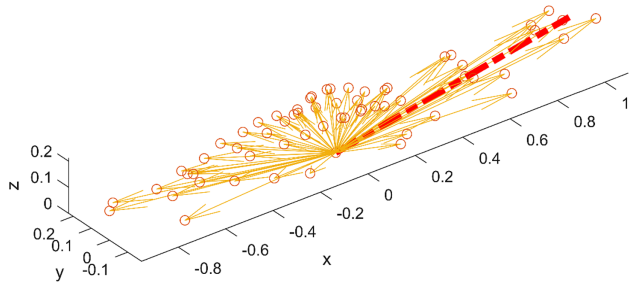

Fig. 6. Example of the resulting BRDF for an angle of incidence (θ_i, φ_i) of (80°, 0°) for road marking sample 1. The incident vector is shown with the red dashed line and has a length of 1 sr^{-1}. The absolute BRDF values are represented by a dot, and the corresponding viewing direction is indicated by an arrow.

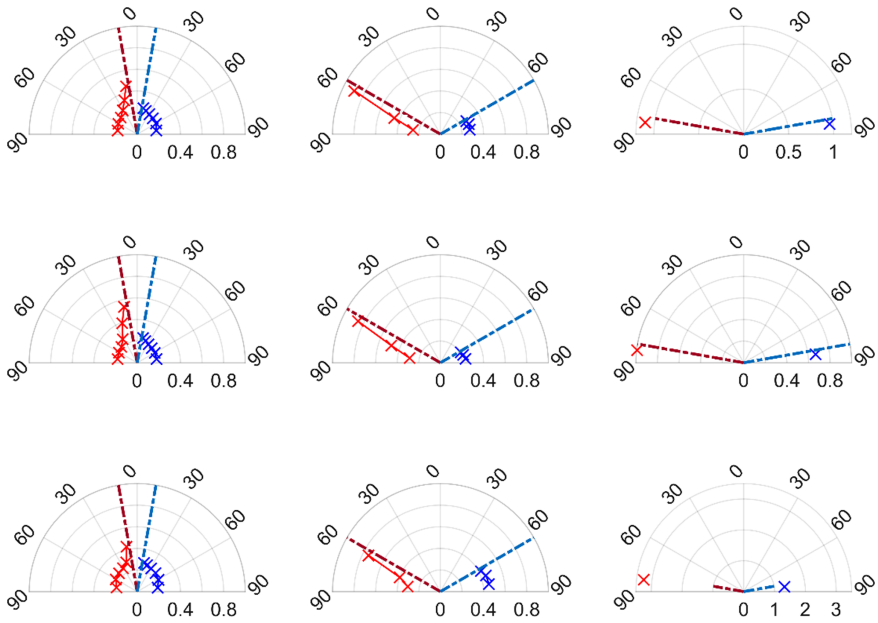

Fig. 7. Polar plots of the BRDF values where the red crosses and dashed lines indicate the retroreflective hemisphere and the blue crosses and dashed lines the specular hemisphere. The dotted red lines indicate the incident vectors that are given a length of 1 sr^{-1}. Plotted on the top row for sample 1, middle row for sample 2, and on the bottom row for sample 3; the three plots in a row represent an incident angle of $\theta_i = 10°$, 60°, and 80° for a fixed $\varphi_i = 0°$, from left to right, respectively. The radius of the polar diagrams is in sr^{-1}, and the angles in the polar diagrams represent the θ angles in degrees.

To make the elementary retro- and specular reflections more visible, the BRDF values are also plotted in polar diagrams with the perimeter representing the various viewing directions. Figure 7 shows an example at a fixed φ_o of 0° and 180°, and for the incident angles $\theta_i = 10°$, 60° and 80° for a fixed φ_i of 0°. The polar diagram is in the plane of $\varphi_o = 0°$ (on the left) and $\varphi_o = 180°$ (on the right). In addition, the dotted blue lines indicate the (ideal) specular reflection vectors. These (ideal) specular reflection vectors are also 1 sr^{-1} in length. The BRDF values in sr^{-1} are indicated with crosses. The red crosses indicate the BRDF values for a φ_o of 0° (retroreflective hemisphere), and the blue crosses indicate the BRDF values for a φ_o of 180° (specular hemisphere).

The general observation of all measured BRDF values is that the retroreflection increases as the incident angle θ_i increases (see Fig. 7). Furthermore, it is noteworthy that, with the larger angles of incident θ_i, in addition to an increasing retroreflection, the specular reflection also increases (see Figs. 6 and 7). In general, for incident angles of $\theta_i > 80°$ and $\varphi_i = 0°$, the BRDF value in the direction of the retroreflection is close to or greater than 1.

6. OPTIMIZATION OF A BRDF MODEL

To describe the measured data of the retroreflective glass bead road markings for further use, we need a BRDF model that summarizes the data accurately. Therefore, in this section, we first explore to what extent an existing generic BRDF model fits the data and then adapt the model where needed.

Since the data exhibit a peaked (retro)reflective cosine-lobe-like behavior, we investigated the Phong model modified for energy conservation. We also considered a classic Fresnel reflection, but that turned out to provide a worse fit to our data than the modified cosine-lobe Phong model. The modified Phong model only exhibits a peaked specular reflective cosine-lobe, but not any retroreflective behavior. Therefore, this model is extended such that a second peaked cosine-lobe is added in the direction of the incident light vector for retroreflection,

$$f_r(\theta_i, \varphi_i, \theta_o, \varphi_o) = \frac{k_d}{\pi} + \frac{k_s(n+2)}{2\pi}(i_s \cdot o)^n + \frac{k_r(n+2)}{2\pi}(i \cdot o)^n, \tag{14}$$

where k_r is the parameter for retroreflection with energy conservation fulfilling the constraint $k_d + k_s + k_r < 1$, and i is the incident unit vector. This BRDF model applies a specular and retroreflective cosine-lobe, where the maximum value is irrespective of the incident angle. However, as mentioned before, the measured BRDF values increase with an increase in the incident angle, which can be integrated in the model by making the parameters k_r and k_s dependent on the incident angle θ_i. Our measured data also indicate a difference in only the length of the cosine-lobe and not so much in its width. Since the diffuse component does not change much with changes in the incident angle, the parameters k_d and n can remain constant. This results in

$$f_r(\theta_i, \varphi_i, \theta_o, \varphi_o) = \frac{k_d}{\pi} + \frac{k_s(\theta_i)(n+2)}{2\pi}(i_s \cdot o)^n + \frac{k_r(\theta_i)(n+2)}{2\pi}(i \cdot o)^n. \tag{15}$$

To determine the best function for $k_r(\theta_i)$ and $k_s(\theta_i)$, the measurement results of road marking sample 1 were taken,

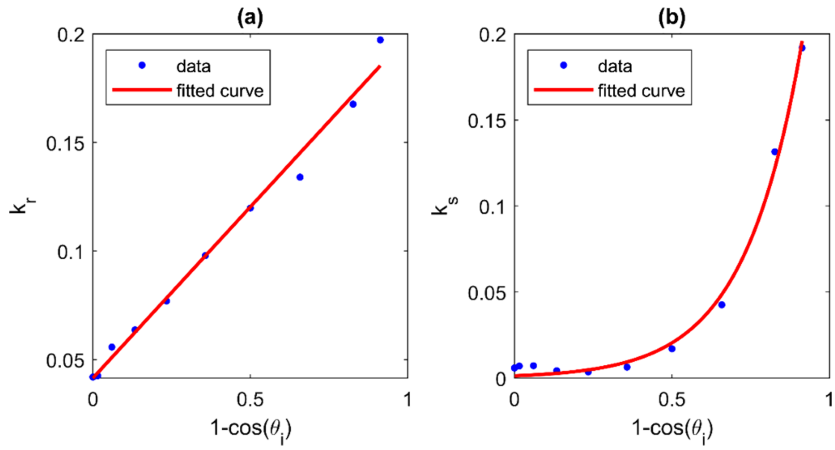

Fig. 8. (a) k_r- and (b) k_s- values resulting from the optimization plotted against $1 - \cos(\theta_i)$ indicated by the blue dots. The solid red line indicates the fit to the data points.

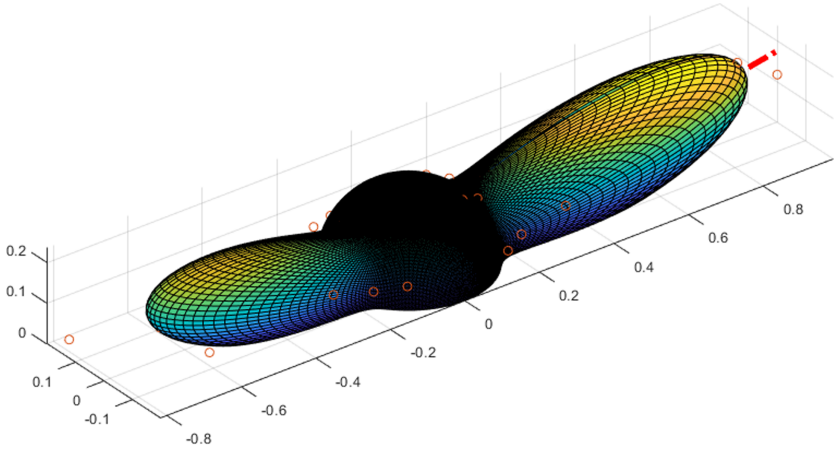

Fig. 9. Example of the fitted BRDF (colored grid) for an angle of incidence (θ_i, φ_i) of (80°, 0°) for road marking 1. The incident vector is shown with the red dashed line and is 1 sr^{-1} in length. The measured BRDF values for each viewing angle are relative to the length of the incident vector and shown by the dots.

and the k_r, k_s, k_d, and n parameters were determined for a randomly chosen incident angle (i.e., θ_i of 80° and a φ_i of 0°) by minimizing the root mean squared error (RMSE) between the calculated $f_r(\theta_o, \varphi_o)$-values using Eq. (15) and the measured $f_m(\theta_o, \varphi_o)$-values. The RMSE is given by

$$\text{RMSE} = \sqrt{\frac{1}{N}\sum_{\theta_o,\varphi_o}\left(f_m(\theta_o, \varphi_o) - f_r(\theta_o, \varphi_o)\right)^2}, \tag{16}$$

where N is the total number of viewing angles. The optimization was done in MATLAB with the Global Optimization Toolbox using the Genetic Algorithm with no constraints. This resulted in a k_r of 0.168, k_s of 0.132, a k_d of 0.620, and n of 24.0 with a RMSE of 0.106. In a next step, the optimization was repeated for all other incident angles, but then with the parameters k_d and n fixed at 0.620 and 24.0. The resulting k_r- and k_s-values are plotted against $1 - \cos(\theta_i)$ in Figs. 8(a) and 8(b), respectively. The RMSE of the fit was lower than 0.185 for all incident angles. The k_r-values were higher than the k_s-values except at θ_i of 85°, meaning that the retroreflection was larger than the specular reflection except at θ_i of 85°.

The k_r-values in Fig. 8(a) could be fitted with a simple linear function,

$$k_r(\theta_i) = k_1(1 - \cos(\theta_i)) + k_2, \tag{17}$$

resulting in a R^2 of 0.99 with the parameters k_1 and k_2 being equal to 0.158 and 0.0415, respectively. The k_s-values in Fig. 8(b) were fitted with a simple exponential function,

$$k_s(\theta_i) = k_3 e^{k_4(1-\cos(\theta_i))}, \tag{18}$$

resulting in a R^2 of 0.99 with the parameters k_3 and k_4 being equal to 0.00133 and 5.467, respectively. The full BRDF model according to Eq. (15), using Eqs. (17) and (18) and the optimized parameters, is plotted for the data at an angle of incidence (θ_i, φ_i) of (80°, 0°) for road marking 1 (so, the measurement data shown in Fig. 6) in Fig. 9.

To quantify the goodness of fit of the BRDF model, we also calculated the normalized root mean squared error (NRMSE) and the normalized cross correlation ratio (NCC) [19]. The NCC and NRMSE are defined as

Table 3. Selected θ Viewing Angles Chosen for Each Selected φ Viewing Angle in Degrees, for an Angle of Incidence of $\varphi_i = 0°$ and $\theta_i = 0°$

RetroPhong									
RM	**RMSE**	**NRMSE**	**NCC**	k_d	n	k_1	k_2	k_3	k_4
1	0.102	0.0370	0.879	0.620	24.0	0.158	0.0415	0.00133	5.47
2	0.106	0.0201	0.861	0.594	24.0	0.0696	0.0733	6.58e-05	8.74
3	0.280	0.0216	0.814	0.701	68.0	0.184	1.53e-12	0.00570	3.40

Table 4. RMSE, NRMSE, and NCC for the RetroPhong Model for Road Markings 2 and 3 Using the Optimized Parameters of Road Marking 1

RetroPhong									
RM	**RMSE**	**NRMSE**	**NCC**	k_d	n	k_1	k_2	k_3	k_4
2	0.121	0.0251	0.837	0.620	24.0	0.158	0.0415	0.00133	5.47
3	0.361	0.0247	0.757	0.620	24.0	0.158	0.0415	0.00133	5.47

Table 5. RMSE, NRMSE, and NCC for the RetroPhong Model for Road Markings 2 and 3 Using the Optimized Parameters of Road Marking 1

RetroPhong									
RM	**RMSE**	**NRMSE**	**NCC**	k_d	n	k_1	k_2	k_3	k_4
1	0.102	0.0370	0.879	0.620	24.0	0.158	0.0415	0.00133	5.47
RetroPhong without specular component									
RM	**RMSE**	**NRMSE**	**NCC**	k_d	n	k_1	k_2	k_3	k_4
1	0.172	0.0308	0.614	0.620	24.0	0.158	0.0415	–	–

$$\mathrm{NCC} = \frac{\sum_{\theta_i,\varphi_i,\theta_o,\varphi_o}\left[\left(f_m(\theta_i,\varphi_i,\theta_o,\varphi_o)-\overline{f_m}\right)\left(f_r(\theta_i,\varphi_i,\theta_o,\varphi_o)-\overline{f_r}\right)\right]}{\sqrt{\sum_{\theta_i,\varphi_i,\theta_o,\varphi_o}\left(f_m(\theta_i,\varphi_i,\theta_o,\varphi_o)-\overline{f_m}\right)^2\sum_{\theta_i,\varphi_i,\theta_o,\varphi_o}\left(f_r(\theta_i,\varphi_i,\theta_o,\varphi_o)-\overline{f_r}\right)^2}}, \tag{19}$$

$$\mathrm{NRMSE} = \frac{\sum_{\theta_i,\varphi_i,\theta_o,\varphi_o}\sqrt{\left[f_m(\theta_i,\varphi_i,\theta_o,\varphi_o)-f_r(\theta_i,\varphi_i,\theta_o,\varphi_o)\right]^2}}{\max(f_m,\ f_r)\,N}, \tag{20}$$

with $\overline{f_r}$ and $\overline{f_m}$ the modeled and measured BRDF values, respectively, averaged over all incident and viewing angles. The max-function is defined as the maximum over all f_m and f_r values. The NCC is a measure of similarity and varies between 0 and 1, with 0 indicating no correlation (0%) and 1 indicating a perfect match (100%) between the relative shape of the BRDF model and measured values [20]. The RMSE, NRMSE, NCC, and the optimization parameters are summarized in Table 3 for the BRDF model, defined through Eqs. (15), (17), and (18) (hereafter referred to as "*RetroPhong*" model) optimized to the data of road marking sample 1, 2, and 3.

Additionally, to check the validity of the model, a cross-validation is performed, where the RMSE, NRMSE, and NCC are calculated for the RetroPhong model optimized to the data of road marking 1, and applied to the data of road marking 2 and 3 (as shown in Table 4).

In this cross-validation, the increase in RMSE and NRMSE, and the decrease in NCC, is quite small between using optimized parameters of road marking sample 1 for road marking sample 2 on the one hand or using the optimized parameters for road marking sample 2 on the other hand (i.e., 0.121, 0.0251, and 0.837 compared to 0.106, 0.0201, and 0.861, respectively). This means that the RetroPhong model parameters that have been optimized to the data of road marking sample 1 can also be effective in predicting the BRDF values of road marking sample 2. For road marking sample 3, the RMSE, NRMSE, and NCC differences are larger, meaning that the set of parameters determined by the optimization of road marking sample 1 are less suitable in predicting the BRDF values of road marking sample 3. It is worth noting that road marking samples 1 and 2 are both Limboplast D480 samples and are, therefore, different from road marking sample 3. Road marking 1 and 2 are cold plastics, whereas road marking sample 3 is a preformed tape with a special polyurethane top coating.

Furthermore, the effect on the RMSE, NRMSE, and NCC when excluding the specular component in Eq. (15) was investigated and is given in Table 5. Excluding the specular component allows us to compare the retroreflective component of the RetroPhong model with other retroreflective models that exclude specular reflection (see below). When excluding the specular component from the RetroPhong model, the RMSE increases by 0.070, and the NRMSE and NCC decrease by 0.0062 and 0.265, respectively. Thus, the specular component does seem to have some added value to the RetroPhong model.

7. BENCHMARKING OF THE RETROPHONG MODEL

The RetroPhong model actually is similar to the Lafortune model, one of the models described in the paper by Belcour *et al*. [10], but here specifically defined for the condition of one retroreflective and one specular lobe. In addition, we added the modeling of k_s and k_r as a function of the incident angle [i.e., Eqs. (17) and (18)] to this specific Lafortune model, resulting in the so-called RetroPhong model. This is benchmarked against four other parametric BRDF models: an improved classical Lambertian model introduced by Oren and Nayar [21], an updated Blinn lobe, an updated Beckmann distribution, and an updated ABC distribution, all introduced by Belcour *et al*. [10] and updated by including retroreflection ($\frac{k_d}{\pi} + f_r + f_b$). The Oren–Nayer parametric BRDF model was included in the benchmark because of its retroreflective property with increasing surface roughness and its ability to explain the view-dependent reflective properties of matte surfaces with geometric optics. The updated Blinn, updated Beckmann, and updated ABC distribution were included based on the similarities in reflective properties of the road markings with the retroreflective gray, yellow, and orange tape used in the study by Belcour *et al*. [10]. Likewise, in the optimization of the RetroPhong model, the parameters in the BRDF models were optimized to minimize the RMSE with the measured data. For the optimization, we again used the Genetic Algorithm of the Global Optimization Toolbox of MATLAB. An overview of the RMSE, NRMSE, and NCC for each BRDF model is given in Table 6.

From these benchmarked models, the ABC-Retro model comes closest to the RetroPhong model with a RMSE around 0.19 and a NRMSE less than 0.09; the NCC is higher than 0.4 for road marking sample 1, but lower than 0.3 for road marking samples 2 and 3. Worth mentioning is that the Beckmann-Retro model outperforms the RetroPhong model in terms of higher NCC for road marking sample 1, but nonetheless it has a higher RMSE and NRMSE. So, all models result in higher RMSE and NRMSE values for all three road marking samples when compared to the RetroPhong model. Even when only considering the retroreflective component of RetroPhong model, as suggested in Table 5, the RMSE and NRMSE are lowest for

Table 6. RMSE, NRMSE, and NCC Parameters for Each Road Marking and BRDF Model

Road Marking 1	RMSE	NRMSE	NCC	Number of Coefficients
RetroPhong	0.102	0.0370	0.879	6
Oren–Nayar	0.203	0.0515	0.310	2
Beckmann-Retro	0.160	0.0676	0.615	3
Blinn-Retro	0.194	0.0871	0.285	3
ABC-Retro	0.116	0.0477	0.819	8
Road marking 2	**RMSE**	**NRMSE**	**NCC**	**Number of Coefficients**
RetroPhong	0.106	0.0201	0.861	6
Oren–Nayar	0.203	0.0820	0.399	2
Beckmann-Retro	0.171	0.0475	0.582	3
Blinn-Retro	0.197	0.0547	0.316	3
ABC-Retro	0.125	0.0305	0.804	8
Road marking 3	**RMSE**	**NRMSE**	**NCC**	**Number of Coefficients**
RetroPhong	0.280	0.0216	0.814	6
Oren–Nayar	0.415	0.0428	0.508	2
Beckmann-Retro	0.490	0.0396	0.581	3
Blinn-Retro	0.487	0.0393	0.219	3
ABC-Retro	0.224	0.0181	0.886	8

Table 7. Optimization Coefficients for Each Road Marking and BRDF Model

Oren–Nayar	α_m	ρ					
Road marking 1	0.865	0.268					
Road marking 2	0.705	0.275					
Road marking 3	1.26	0.470					
Beckmann-Retro	k_d	α	R_0				
Road marking 1	0.796	8.20	0.995				
Road marking 2	0.822	9.36	0.993				
Road marking 3	0.996	1.61e3	1.00				
Blinn-Retro	k_d	α_b	α_r				
Road marking 1	0.919	2.77e3	7.91e3				
Road marking 2	0.881	2.50e3	7.10e3				
Road marking 3	0.993	6.72e3	1.65e4				
ABC-Retro	k_d	R_0	A_b	B_b	C_b	A_r	B_r	C_r
Road marking 1	0.534	0.0472	1.82	13.5	1.51	1.02	0.0775	6.97
Road marking 2	0.0303	0.140	1.59	32.6	1.08	1.19	0.00779	0.0179
Road marking 3	0.747	0.00466	6.66	37.8	0.710	3.58	22.9	0.729
RetroPhong	k_d	n	k_1	k_2	k_3	k_4		
Road marking 1	0.620	24.0	0.158	0.0415	0.00133	5.47		
Road marking 2	0.594	24.0	0.0696	0.0733	6.58e−05	8.74		
Road marking 3	0.701	68.0	0.184	1.53e−12	0.00570	3.40		

the RetroPhong model, though the differences with the other BRDF models become smaller. Regarding NCC, the highest values are found for the RetroPhong model, with the exception of the Beckmann-Retro model for road marking 1.

Finally, all optimization coefficients are documented in Table 7 for all three road markings and all BRDF models.

8. DISCUSSION

The new RetroPhong model shows good agreement with the measured reflectivity of the three road markings containing glass beads and for the wide set of incident and viewing angles used in this study. As we focus on road markings illuminated by road lighting, for which different angles of incident and viewing angles are relevant than for illumination by car headlights, we did not measure the incident angles and viewing angles as specified in the CIE 54.2 [2] report. In this paper, the maximum polar incident angle was for practical reasons limited to 85°, implying that it is still unclear how well the RetroPhong model predicts reflectivity beyond this angle. We set the limitation to 85° because the measurements beyond this incident angle would become too noisy to accurately determine a BRDF value in our measurement setup. Nonetheless, when comparing the BRDF value given by the RetroPhong model for the particular incidence (88.8°) and viewing (87.7°) angle with the BRDF value as required in EN1436 [3], retrieved by converting the R_l value of the technical data sheet, it is found that for road marking 2 the difference in BRDF values is relatively small (<0.13), whereas the difference is larger for road markings 1 and 3 (0.63 and 0.91, respectively). Furthermore, the RetroPhong model was checked regarding energy conservation, meaning that the sum of the diffuse, specular, and retroreflective parameters ($k_d + k_s + k_r$) should be less than 1. This does seem to be the case within the measurement range of this study; however, this is violated when extrapolating toward $\theta_i > 85°$. This implies that the functions that are shown in Fig. 8 based on Eqs. (17) and (18) most likely show a falloff in specular and retroreflective parameters toward reaching 90°. Since we did not measure beyond a polar incident angle of 85°, it is still uncertain what the exact behavior of these parameters would be beyond this angle. However, this is not a severe limitation for this study since we focus on a suitable BRDF model for road markings illuminated by road lighting (i.e., luminaires).

From all (retro)reflective BRDF models evaluated in this study, in general, the RetroPhong model fits our data best. Also, when excluding the specular component from the RetroPhong model, it still shows a better agreement with the data than the existing (retro)reflective BRDF models of the benchmark. It is worth mentioning that in this particular case the RetroPhong model includes six optimization parameters, whereas the other BRDF models use between one and eight optimization parameters.

9. CONCLUSION

By measuring three glass beads embedded road marking samples for a larger set of incident and viewing angles, BRDF values relevant for road lighting (i.e., illumination by luminaires) are reported. The BRDF values are determined using a commercial LNFG adapted to our needs and equipped with an imaging luminance measurement device.

Based on the general observation that the BRDF values in the specular and retroreflection region increase as the angle of incidence increases and follow a cosine-lobe-like behavior, a new RetroPhong BRDF model was created. In this model, the retroreflection is modeled by a cosine-lobe in the direction of the incident vector, with the peak of the lobe increasing with the theta incident angle. The increase in specular reflection is modeled by a cosine-lobe in the direction of the specular direction, with the peak of the lobe also increasing with the polar incident angle.

To determine the relevance and relative "goodness" of fit to the data, the RetroPhong BRDF model was benchmarked to four other (retro)reflective BRDF models: Oren–Nayar, Beckmann-Retro, Blinn-Retro, and ABC-Retro. The RMSE and NRMSE were found to be the lowest for the RetroPhong model for each road marking when compared to these other models. The NCC was found highest for the RetroPhong model with the exception of the Beckmann-Retro model for road marking 1. In general, it can be concluded that the RetroPhong model fits the measurements better than the other models.

In order to allow the new model to be used in rendering software, some practical implementation steps need to be taken. An example of how to implement the RetroPhong model in a PBR such as Mitsuba [22] can be found in the Appendix A.

Future work will be to examine and parametrize the RetroPhong model for more and different sets of retroreflective materials and to extend the angles of incidence beyond 85° in order to reach a fully generic model. Such a generic model would be of great use for improving the accuracy of modeling the visibility of road markings illuminated by both road lighting luminaires and car headlights in PBRs such as Mitsuba.

APPENDIX A

In this appendix, the most relevant additions to the Mitsuba physical-based renderer for the successful use of the new RetroPhong model are provided. The current coding of the modified Phong BRDF model plugin in Mitsuba was altered to include the specular and retroreflection as described in the RetroPhong model [Eq. (15)]. Mitsuba is a free software under the GNU general public license and copyrighted by Jakob and others [22]. Any original Mitsuba code (i.e., modified Phong BRDF model) that is shown in this appendix is to the credit of Jakob and others.

In Mitsuba, the functions for the evaluation of BSDF sampling, the probability distribution function, and the hardware shader implementation used for the implementation of the modified Phong reflectance model have been adapted to the RetroPhong model.

The function to determine the specular reflection of the current fragment of the evaluation of BSDF sampling of the modified Phong BRDF model in Mitsuba given by

```
if (hasSpecular) {
        Float alpha = dot(bRec.wo, reflect(bRec.wi)),
        exponent = m_exponent->eval(bRec.its).average();
```

(Table continued)

```
        if (alpha > 0.0f) {
            result += m_specularReflectance->eval(bRec.its) *
                ((exponent + 2) * INV_TWOPI * std::pow(alpha,
                exponent));
        }
}
```

declares the result similar to Eq. (3).

This function was altered to include retroreflection, where the new fragment of the evaluation of BSDF sampling declares the result according to Eq. (15):

```
if (hasSpecular) {
        Float alphaS = dot(bRec.wo, reflect(bRec.wi)),
        exponent = m_exponent-> eval(bRec.its).average();

        if (alphaS > 0.0f) {
                result += (m_specularReflectance_k1->
                eval(bRec.its) * ((1 - Frame::cosTheta(bRec.wi)))
                +m_specularReflectance_k2-> eval(bRec.its))*
                ((exponent + 2) * INV_TWOPI * std::pow(alphaS,
                exponent));
        }
}
if (hasRetro) {
        Float alphaR = dot(bRec.wo, bRec.wi),
        exponent = m_exponent-> eval(bRec.its).average();

        if (alphaR > 0.0f) {
                result += (m_retroReflectance_k3-> eval(bRec.its) *
                (math::fastexp((1 - Frame::cosTheta(bRec.wi)) *
                m_retroReflectance_k4-> eval(bRec.its))))
                * ((exponent + 2) * INV_TWOPI * std::pow(alphaR,
                 exponent));
        }
}
```

In addition, similarly, although differently defined, the function for the probability density function of the current fragment of the modified Phong BRDF model in Mitsuba given by

```
if (hasSpecular) {
        Float alpha = dot(bRec.wo, reflect(bRec.wi)),
        exponent = m_exponent->eval(bRec.its).average();

        if (alpha > 0){
                specProb = std::pow(alpha, exponent) * (exponent +
                2.0f) / (2.0f * M_PI);
        }
}
```

also following Eq. (3).

Again this function was altered to include retroreflection, to which the new snippet follows Eq. (15):

```
if (hasSpecular) {
        Float alphaS = dot(bRec.wo, reflect(bRec.wi)),
        exponent = m_exponent->eval(bRec.its).average();
        if (alphaS > 0){
                specProb = (m_specularReflectance_k1->eval
                (bRec.its) * ((1 - Frame::cosTheta(bRec.wi))) +
                m_specularReflectance_k2->eval(bRec.its)) *
                (((exponent + 2.0f) / (2.0f * M_PI)) * std::pow
                (alphaS, exponent));
        }
}
if (hasRetro) {
        Float alphaR = dot(bRec.wo, bRec.wi),
        exponent = m_exponent->eval(bRec.its).average();

        if (alphaR > 0){
                retroProb = (m_retroReflectance_k3->eval(bRec.its)
                        * (math::fastexp((1 - Frame::cosTheta
                        (bRec.wi))* m_retroReflectance_k4
                        ->eval(bRec.its)))* (((exponent + 2.0f)
                        / (2.0f * M_PI)) * std
                        ::pow(alphaR, exponent));
        }
}
```

For the Mitsuba hardware shader implementation, the current fragment of the modified Phong BRDF model in Mitsuba returns the vector according to Eq. (3), in OpenGL shading language:

```
oss << "vec3 " << evalName << "(vec2 uv, vec3 wi, vec3 wo) { " << endl
    << "   if (cosTheta(wi) <= 0.0 || cosTheta(wo) <= 0.0)" << endl
    << "      return vec3(0.0);" << endl
    << "   vec3 R = vec3(-wi.x, -wi.y, wi.z);" << endl
    << "   float specRef = 0.0, alpha = dot(R, wo);" << endl
    << "   float exponent = min(30.0, " << depNames[0] << "(uv)[0]);"
       << endl
    << "   if (alpha > 0.0)" << endl
    << "      specRef = pow(alpha, exponent) * " << endl
    << "      (exponent + 2) * 0.15915;" << endl
    << "   return (" << depNames[1] << "(uv) * inv_pi" << endl
    << "          + " << depNames[2] << "(uv) * specRef) *
          cosTheta(wo);" << endl
    << "}" << endl
    << "vec3 " << evalName << "_diffuse(vec2 uv, vec3 wi, vec3 wo) {"
      << endl
    << "      if (wi.z <= 0.0 || wo.z <= 0.0)" << endl
    << "          return vec3(0.0);" << endl
    << "      return " << depNames[1] << "(uv) * (inv_pi * cosTheta
         (wo));" << endl
    << "}" << endl;
```

The modified fragment to include retroreflection returns the vector according to Eq. (15):

```
oss << "vec3 " << evalName << "(vec2 uv, vec3 wi, vec3 wo) {" << endl
    << "   if (cosTheta(wi) <= 0.0 || cosTheta(wo) <= 0.0)" << endl
    << "      return vec3(0.0);" << endl
    << "   vec3 R = vec3(wi.x, wi.y, wi.z);" << endl
    << "   vec3 S = vec3(-wi.x, -wi.y, wi.z);" << endl
    << "   float retroRef = 0.0, alphaR = dot(R, wo);" << endl
    << "   float specRef = 0.0, alphaS = dot(S, wo);" << endl
    << "   float exponent = min(30.0, " << depNames[0] << "(uv)[0]);"
       << endl
    << "   if (alphaS > 0.0)" << endl
    << "      specRef = pow(alphaS, exponent) * " << endl
    << "   (exponent + 2) * 0.15915;" << endl
    << "   if (alphaR > 0.0)" << endl
    << "      retroRef = pow(alphaR, exponent) * " << endl
    << "   (exponent + 2) * 0.15915;" << endl
    << "   return (" << depNames[1] << "(uv) * inv_pi" << endl
    << "           + (" << depNames[2] << "(uv) * (1-cosTheta(wi))
          <<endl
    << "           + " << depNames[3] << "(uv)) * specRef" << endl
    << "           + (" << depNames[4] << "(uv) * exp(" <<
          depNames[5] << "(uv) * (1- << endl
    << "            cosTheta(wi)))) * retroRef) * cosTheta(wo);" << endl
    << "}" << endl
    << "vec3 " << evalName << "_diffuse(vec2 uv, vec3 wi, vec3 wo) {"
       << endl
    << "   if (wi.z <= 0.0 || wo.z <= 0.0)" << endl
    << "      return vec3(0.0);" << endl
    << "   return " << depNames[1] << "(uv) * (inv_pi * cosTheta(wo));"
       << endl
    << "}" << endl;
```

Funding. Rijkswaterstaat.

Acknowledgment. The first author was supported by the Rijkswaterstaat.

Disclosures. The authors declare no conflicts of interest.

Data availability. Data underlying the results presented in this paper are not publicly available at this time but may be obtained from the authors upon reasonable request.

REFERENCES

1. R. C. Bible and N. Johnson, "Retroreflective material specifications and on-road sign performance," Transp. Res. Rec. **1801**, 61–72 (2002).
2. International Commission on Illumination, "Retroreflection: definition and measurement," CIE 54.2-2001 (International Commission on Illumination, 2001).
3. European Committee for Standardization, "Road marking materials-road marking performance for road users," CEN. Report No: CEN-EN 1436: 1999 (1999).
4. International Commission on Illumination, "Roadsigns," CIE 74-1988 (International Commission on Illumination, 1988).
5. European Committee for Standardization, "European Standard: Fixed, vertical road traffic signs," CEN. Report No: CEN-EN 12899: 2007 (2007).
6. European Committee for Standardization, "High visibility clothing–test methods and requirements," CEN. Report No: CEN-EN-ISO 20471: 2013 (2013).
7. M. Sato and T. Hagio, "Visibility enhancement and power saving by pro-beam LED tunnel lighting method," J. Light Visual Environ. **38**, 89–93 (2014).
8. M. Kimura, Y. Hamada, Y. Ikeda, H. Motomura, and M. Jinno, "Importance of a vector component and the vertical illuminance in road lighting for the obstacle visibility of the road," J. Sci. Technol. Lighting **42**, 17–21 (2019).
9. F. E. Nicodemus, J. C. Richmond, J. J. Hsia, I. W. Ginsberg, and T. Limperis, "Geometrical considerations and nomenclature for reflectance," NBS Monograph 160 (National Bureau of Standards, 1992).
10. L. Belcour, R. Pacanowski, M. Delahaie, A. Laville-Geay, and L. Eupherte, "Bidirectional reflectance distribution function measurements and analysis of retroreflective materials," J. Opt. Soc. Am. A **31**, 2561–2572 (2014).
11. E. P. Lafortune and Y. D. Willems, "The modified Phong reflectance model," in *Using the Modified Phong Reflectance Model for Physically Based Rendering* (Katholieke Universiteit Leuven. Departement Computerwetenschappen, 1994), p. 19.
12. B. Smith, "Geometrical shadowing of a random rough surface," IEEE Trans. Antennas Propag. **15**, 668–671 (1967).
13. P. Beckmann and A. Spizzichino, *The Scattering of Electromagnetic Waves from Rough Surfaces* (Norwood, 1987).
14. C. Schlick, "An inexpensive BRDF model for physically-based rendering," in *Computer Graphics Forum* (Blackwell Science, 1994), Vol. **13**, pp. 233–246.
15. J. F. Blinn, "Models of light reflection for computer synthesized pictures," in *Proceedings of the 4th Annual Conference on Computer Graphics and Interactive Techniques* (1977), pp. 192–198.
16. E. L. Church, P. Z. Takacs, and T. A. Leonard, "The prediction of BRDFs from surface profile measurements," in *Scatter from Optical Components* (SPIE, 1990), Vol. **1165**, pp. 136–150.
17. J. Löw, J. Kronander, A. Ynnerman, and J. Unger, "BRDF models for accurate and efficient rendering of glossy surfaces," ACM Trans. Graph. **31**, 1–14 (2012).
18. F. B. Leloup, S. Forment, P. Dutré, M. R. Pointer, and P. Hanselaer, "Design of an instrument for measuring the spectral bidirectional scatter distribution function," Appl. Opt. **47**, 5454–5467 (2008).
19. J. Audenaert, F. B. Leloup, B. GielVan, G. Durinck, G. Deconinck, and P. Hanselaer, "Impact of the accurateness of bidirectional reflectance distribution function data on the intensity and luminance distributions of a light-emitting diode mixing chamber as obtained by simulations," Opt. Eng. **52**, 095101 (2013).
20. V. GesuDi and V. Starovoitov, "Distance-based functions for image comparison," Pattern Recognit. Lett. **20**, 207–214 (1999).
21. M. Oren and S. K. Nayar, "Generalization of Lambert's reflectance model," *Proceedings of the 21st Annual Conference on Computer Graphics and Interactive Techniques*, July 1994, pp. 239–246.
22. W. Jakob, "Mitsuba physically based renderer," 2010, https://www.mitsuba-renderer.org/.